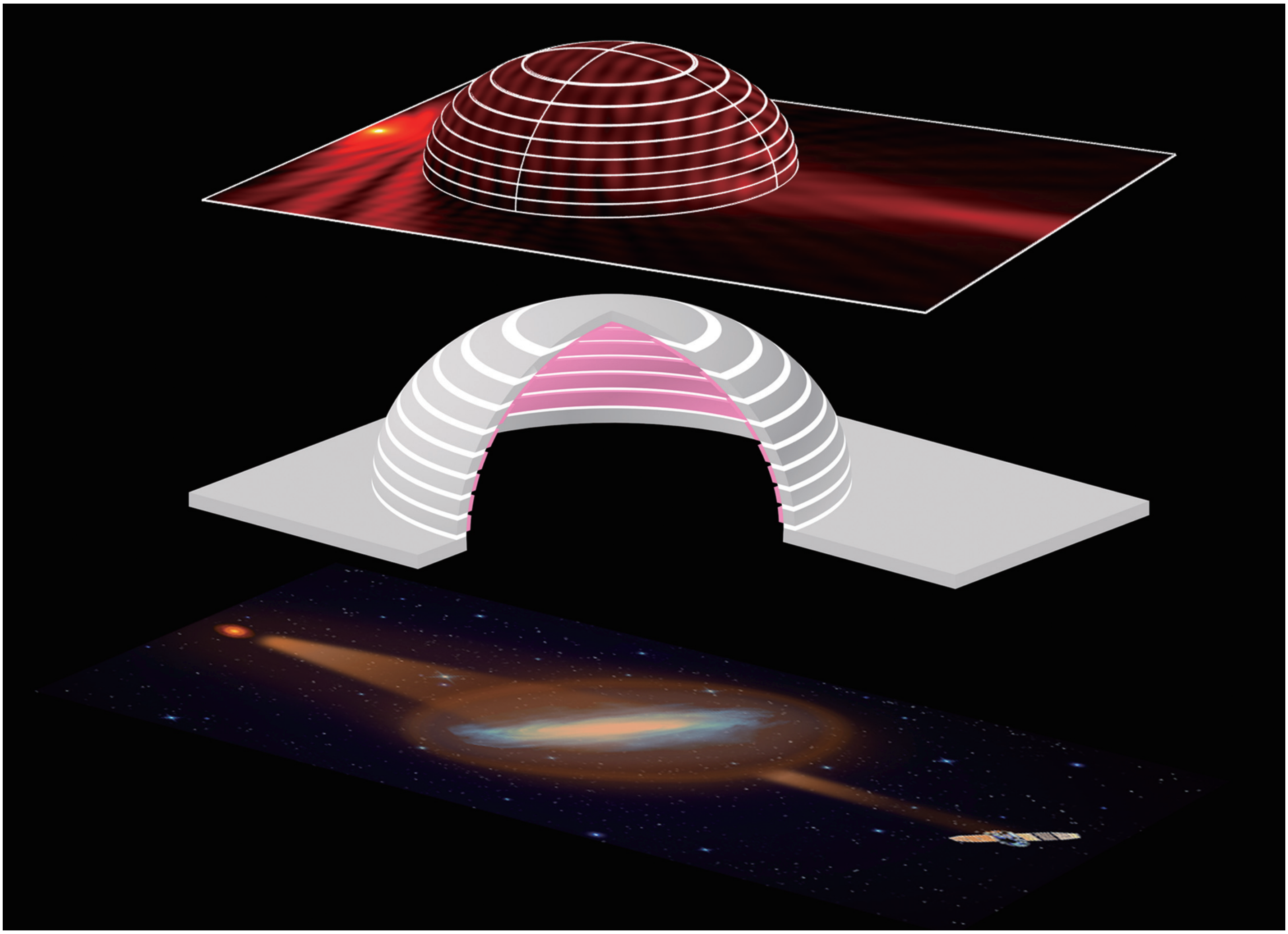

Showcasing research from the School of Optoelectronic Engineering and Instrumentation Science, Dalian University of Technology

A reprogrammable multifunctional chalcogenide guided-wave lens

We illustrate a reconfigurable multi-mode guided-wave lens, composed by a Rinehart shaped curved waveguide with an effective refractive index gradient profile through partially crystallizing $Ge_2Sb_2Te_5$. Upon changing the bias time of the external voltage, the refractive index gradient profile can be tuned with a transformative platform for various functions. The electrically reprogrammable lens can dynamically acquire various functionalities with an ultrafast response time. Our method provides a universal method to obtain ultrafast and highly versatile guided-wave manipulation, such as Einstein rings, cloaking, Maxwell fish-eye lenses and Luneburg lenses.

As featured in:

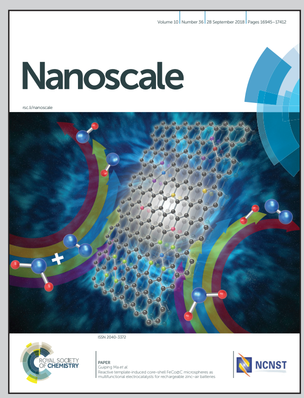

See Tun Cao, Cheng-Wei Qiu *et al.*, *Nanoscale*, 2018, **10**, 17053.

Nanoscale

PAPER

View Article Online
View Journal | View Issue

Check for updates

Cite this: *Nanoscale*, 2018, **10**, 17053

A reprogrammable multifunctional chalcogenide guided-wave lens†

Tun Cao, *[a] Chen-Wei Wei,[a] Meng-Jia Cen,[a] Bao Guo,[a] Yong-June Kim,[b] Shuang Zhang [c] and Cheng-Wei Qiu*[b]

The transformation optics (TO) technique, which establishes an equivalence between a curved space and a spatial distribution of inhomogeneous constitutive parameters, has enabled an extraordinary paradigm for manipulating wave propagation. However, extreme constitutive parameters, as well as a static nature, inherently limit the simultaneous achievement of broadband performance, ultrafast reconfigurability and versatile reprogrammable functions. Here, we integrate the TO technique with an active phase-change chalcogenide to achieve a reconfigurable multi-mode guided-wave lens. The lens is made of a Rinehart-shaped curved waveguide with an effective refractive index gradient profile through partially crystallizing $Ge_2Sb_2Te_5$. Upon changing the bias time of the external voltage imparted to the $Ge_2Sb_2Te_5$ segments, the refractive index gradient profile can be tuned with a transformative platform for various functions for visible light. The electrically reprogrammable multi-mode guided-wave lens is capable of dynamically acquiring various functionalities with an ultrafast response time. Our findings may offer a significant step forward by providing a universal method to obtain ultrafast and highly versatile guided-wave manipulation, such as in Einstein rings, cloaking, Maxwell fish-eye lenses and Luneburg lenses.

Received 13th March 2018,
Accepted 23rd May 2018

DOI: 10.1039/c8nr02100g

rsc.li/nanoscale

1. Introduction

Modern trends in the development of photonics technology have boosted the requirement for multifunctional optical devices.[1,2] Particularly, the active control of 2D planar metamaterials, so-called metasurfaces, has been intensively investigated.[3,4] It is achieved by incorporating tunable or reconfigurable resonators that are steered *via* a gate voltage bias,[5,6] thermal heating[7] or mechanical actuation[8,9] into the metasurface design. This has led to interesting applications like reconfigurable antennae,[10] tunable absorbers,[11–13] beam modulators[14] and chirality controllers.[15,16] Notably, recent works have demonstrated emerging developments in transformation optics (TO)[17] such as cloaking,[18,19] lens focusing[20,21] and light concentration and manipulation.[22,23] Nevertheless all the proposed TO devices are static thus far, and most of them can only perform a single function. Although switchable TO devices capable of demonstrating multiple functionalities in real time are significantly more favorable for practical applications, their realization remains a great challenge, especially in the visible range, due to the complexity of controlling the material properties through external stimuli in an integrated way and the scarceness of active materials with strong index modulation in the visible region. Herein, we propose a novel approach to design switchable multi-functional TO devices to control guided-wave propagation dynamically. The key to our approach is to map a gradient index lens onto a rotationally symmetric Rinehart-shaped surface consisting of multilayered phase-change chalcogenide (*i.e.* $Ge_2Sb_2Te_5$) segments. The proposed device features broadband operation, ultrafast reconfigurability and a combination of various reprogrammable functions in a single thin nonplanar TO structure in the visible region.

$Ge_2Sb_2Te_5$, a classical chalcogenide glass, has been widely investigated in rewritable optical data storage and non-volatile electronic memory as it has an ultrafast switching time (<500 ps), a considerable number of rewriting cycles (>10^8 times) before failure and excellent thermal stability.[24–26] Remarkably, recent works have experimentally demonstrated that very large variations in the refractive index of $Ge_2Sb_2Te_5$

[a] *School of Optoelectronic Engineering and Instrumentation Science, Dalian University of Technology, 116024, China. E-mail: caotun1806@dlut.edu.cn*
[b] *Department of Electrical and Computer Engineering, National University of Singapore, 4 Engineering Drive 3, Singapore 117583, Republic of Singapore. E-mail: eleqc@nus.edu.sg*
[c] *School of Physics and Astronomy, University of Birmingham, Birmingham B15 2TT, UK*

† Electronic supplementary information (ESI) available: Derivation of the refractive index profile of the curvature, refractive index of $Ge_2Sb_2Te_5$ in different structural phases, "on/off" state of the multi-functions of the Rinehart-shaped surface, the multi-functions of the Rinehart-shaped surface with different discretization processes, the multi-functions of the Rinehart-shaped surface at different wavelengths, the conditions of the $Ge_2Sb_2Te_5$ slabs for the various functions, and a description of the supporting movie. See DOI: 10.1039/c8nr02100g

can be obtained in the visible-infrared region as its phase transitions between amorphous and crystalline.[27] In particular, it has been shown that $Ge_2Sb_2Te_5$ based metasurfaces are promising for reversibly tunable photonic devices.[28–30] In light of this feature, $Ge_2Sb_2Te_5$ was chosen for the design of reconfigurable and reprogrammable 3D TO devices in the visible region. In particular, we demonstrate four singular functions of an Einstein ring,[31] invisible cloaking,[32] a Luneburg lens,[33] and a Maxwell fish-eye lens[34] in one curved surface.

2. Results and discussion

Fig. 1(a) shows a version of the Einstein ring: a renowned phenomenon tracing back to 1936 predicted by general relativity (GR) and explored in astronomy.[35,36] According to GR, gravity causes a deflection of light due to the gravitational field of a massive body (*e.g.* galaxy or star). In this case, the galaxy bends the light emanating from a point source, such as another galaxy or star, which is directly behind it, focusing the otherwise divergent light into a visible ring. That is, curved space caused by the massive galaxy/star results in a gravitational lens, which can gravitationally collimate the diffracting optical beam. This gravitational lensing effect occurs as soon as the light emanating from distant objects is curved or deviated around the massive body. This results in a phenomenon possessing a significant likeness to what happens once light goes through a lens. The Einstein ring is the most straightforward and symmetrical effect of the gravitational lens, which can be generated by perfectly aligning the source, gravitational lens and observer. It corresponds to the case where the observer detects the light diverged by the gravitational lens as if it were a ring or circumference.

In TO, the dielectric constant can be spatially engineered to control the propagation of the wave in the same way as the curvature of space does. Thus, Einstein ring behavior can be mimicked using a graded index lens on a curved surface, which enables the formation of a narrow beam that propagates in a nearly non-diffracting manner over a substantial distance. We show that an existing flat lens can be mapped onto a rotationally symmetric curved surface by varying the refractive index distribution. These two geometries are presented in Fig. 1(b). The first geometry is a planar space with a radius (r) dependent rotationally symmetric refractive index profile ($n(r)$). The second is an arbitrary rotationally symmetric curved surface (C) with a ρ dependent rotationally symmetric refractive index profile ($N(\rho)$), where ρ is the perpendicular distance from the z-axis to C. We used a standard polar coordinate for

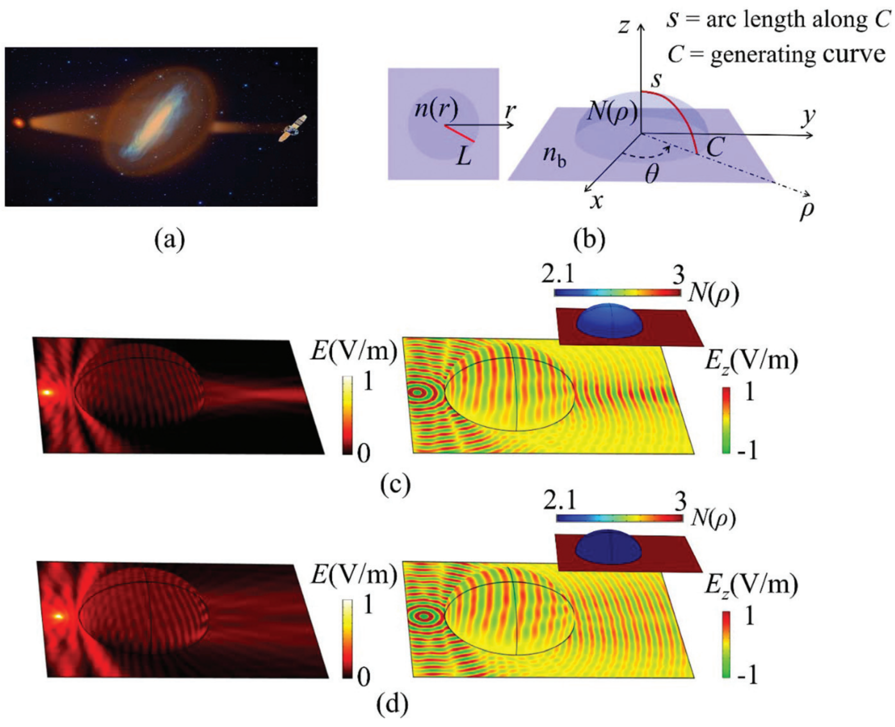

Fig. 1 (a) Picture of an Einstein ring: a beam from a point source is collimated by a gravitational lens, and then observed as a virtual ring around a mass body. (b) Illustration of the paths of a beam (marked in red lines) that are equated for the flat plane (left column) and a rotationally symmetric Rinehart-shaped curved surface (right column). Simulations of the light propagation on the Rinehart-shaped surface, where the incident wave is a point source propagating from left to right. (c) The surface filled with gradient refractive index dielectric that can generate a narrow collimated total E-field $E=\sqrt{|E_x|^2+|E_y|^2+|E_z|^2}$ (left column) and E-field along the z-axis E_z (right column) at λ = 500 nm, where the inhomogeneous area acts as a gravitational lens on the light. (d) The light propagation in the Rinehart-shaped surface filled with homogeneous crystalline $Ge_2Sb_2Te_5$ for beam intensity E (left column) and E_z (right column) at λ = 500 nm. The insets show the curvature with the refractive index distribution of the dielectric ($N(\rho)$) filling the structure.

the planar space and a cylindrical coordinate for the curved surface.

To derive the refractive index profile of the curvature ($N(\rho)$), we slightly modified the approach reported in ref. 18 by equating the radial light path in the flat homogeneous surface L (left column of Fig. 1(b)) with the radial light path in the rotationally symmetric curved surface C (right column of Fig. 1(b)),[37]

$$N(\rho) = n[F(\rho)]F(\rho)/\rho \tag{1}$$

where $F(\rho) = \exp\int_1^{\rho}[s'(\rho)/\rho]\mathrm{d}\rho$ and the arc distance measured along C is denoted $s = \frac{1}{2}\rho + \frac{1}{2}\sin^{-1}\rho$. A detailed derivation of eqn (1) is shown in the ESI.† The phenomenon of an Einstein ring that can produce a narrow collimated beam is demonstrated using a Rinehart-shaped surface composed of dielectric materials with a gradient refractive index profile. The Rinehart-shaped curvature is placed above a ground planar slab. Based on eqn (1), the refractive index profile of the Einstein ring can be expressed as

$$N(\rho) = \frac{2n_{\mathrm{b}}}{\left(1+\sqrt{1-\rho^2}\right)^{\frac{1}{2}}\left(e^{\overline{\left(1+\sqrt{1-\rho^2}\right)^{\frac{1}{2}}}^{\,\rho}} + e^{\overline{\left(1+\sqrt{1-\rho^2}\right)^{\frac{1}{2}}}^{\,-\rho}}\right)} \tag{2}$$

where n_{b} is the refractive index of the ground plane. The refractive indices for different structural states of $Ge_2Sb_2Te_5$ attained from the experimental data[27] are summarized in the ESI (Fig. S1†), and can be used for the refractive index profile.

Fig. 1(c) illustrates a guided wave that propagates on the Reinhart-shaped curvature filled by the $Ge_2Sb_2Te_5$ dielectric. Here, we set the operating wavelength at λ = 500 nm. $N(\rho)$ of $Ge_2Sb_2Te_5$ dielectric was obtained from eqn (2) and the bottom plate was the amorphous $Ge_2Sb_2Te_5$ dielectric (n_{b} = 3). The shell thickness of the curvature was 5 nm (T_{s} = 5 nm). It was confirmed that the gradient distribution of $N(\rho)$ (the inset of Fig. 1(c)) can focus the diverging light propagating through the Reinhart-shaped curvature into a linear non-diffracting fashion. As a control study, we present the performance of the structure filled with homogeneous crystalline $Ge_2Sb_2Te_5$ ($N(\rho)$ = 2.1) in Fig. 1(d). It shows that the curved surface can now strongly diverge the incident light fronts and thus switch off the function of beam collimation. The structure was simulated using the commercial software COMSOL with details shown in the ESI.† It was shown that the $Ge_2Sb_2Te_5$ dielectric was optically lossy over the visible region, owing to the high imaginary part of the refractive index (k_{b}) of $Ge_2Sb_2Te_5$.[38] However in this model, the ultrathin thickness (5 nm) of the $Ge_2Sb_2Te_5$ curvature may lead to negligibly small light absorptance according to the Beer–Lambert law.[39] Therefore, herein we did not take into account the k_{b} of $Ge_2Sb_2Te_5$.

For consideration of the practical experimental realization of the device, the graded refractive index distribution was discretized by dividing the curvature into ν (ν = 9) layers along the z-axis. The simulations on different numbers of segments are summarized in the ESI (Section 4†), and it was confirmed that ν = 9 is sufficient to achieve the proposed functionalities. Every curved layer has an equal arc length and is filled with $Ge_2Sb_2Te_5$ of different partial crystallization ratios accordingly. The total height of the discretized Rinehart-shaped curved surface along the z-axis was 630 nm. The height of each $Ge_2Sb_2Te_5$ constitutive segment was 65 nm along the z-axis. The radius of the bottom of the Rinehart-shaped curved surface was 1000 nm. Fig. 2(a) shows a schematic view of the discretized Rinehart-shaped surface. The crystallization phase of each $Ge_2Sb_2Te_5$ segment is thermally controlled by a current through the bias voltage (V_{bias}) between V_{bias} = 1 V and melt-quenched amorphization at V_{bias} = 3 V on nanosecond (ns) timescales. The bias time (t_{bias}) of the V_{bias} can be controlled through an electrical switch. Nine layers of SiO_2 were introduced to separate the $Ge_2Sb_2Te_5$ slabs to prevent heat transfer between them. Nine individual ITO line cell electrodes were deposited onto the inside surface of each $Ge_2Sb_2Te_5$ segment. As the electric current goes through the ITO filament, the Joule heat causes the chalcogenide to change its structural state. Namely, it enables the electric current to heat up the $Ge_2Sb_2Te_5$ segments independently thus precisely controlling the crystallization ratio for each $Ge_2Sb_2Te_5$ segment.

Fig. 2(b) shows that such a discretization process performed on the continuous refractive index distribution can provide a simple layered structure to approximate the gradient refractive index distribution in eqn (2). This multilayered curvature can conformally cover the bump, in which the total electric surface field $E = \sqrt{|E_x|^2+|E_y|^2+|E_z|^2}$ incident from the left is reconstructed to the right so as to converge the beam into a fine line, as shown in Fig. 2(c). The magnitude of the electric field along the z-axis (E_z) is presented in Fig. 2(d).

To show the multifunctionality of the structure, we present three more examples of TO phenomena (*i.e.* invisible cloaking, the Luneburg lens, and the Maxwell fish-eye lens) which can be realized with the same device by gradually tailoring the refractive index of $Ge_2Sb_2Te_5$ *via* V_{bias}. These unique TO features can all map onto the Rinehart-shaped surface (Fig. 2(a)). For the invisibility cloak design, the refractive index profile is given as

$$N(\rho) = \frac{n_{\mathrm{b}}}{\left(1+\sqrt{1-\rho^2}\right)^{\frac{1}{2}}} \tag{3}$$

where n_{b} = 3.0 corresponding to the amorphous $Ge_2Sb_2Te_5$ ground layer. The right column of Fig. 3(a) shows the performance of the invisible cloaking at λ = 500 nm, where the discretized cloak compensates for the phase difference and reconstructs the cylindrical wavefront of the light propagating through the curvature and subsequently hides the object underneath the bump. Another example is an achievement of the 'monopole' lenses, or the so-called Maxwell fish-eye. This shows the function of redirecting the outgoing beam from a point source to create a second focal point on the opposite side of the lens when the point source is placed on the per-

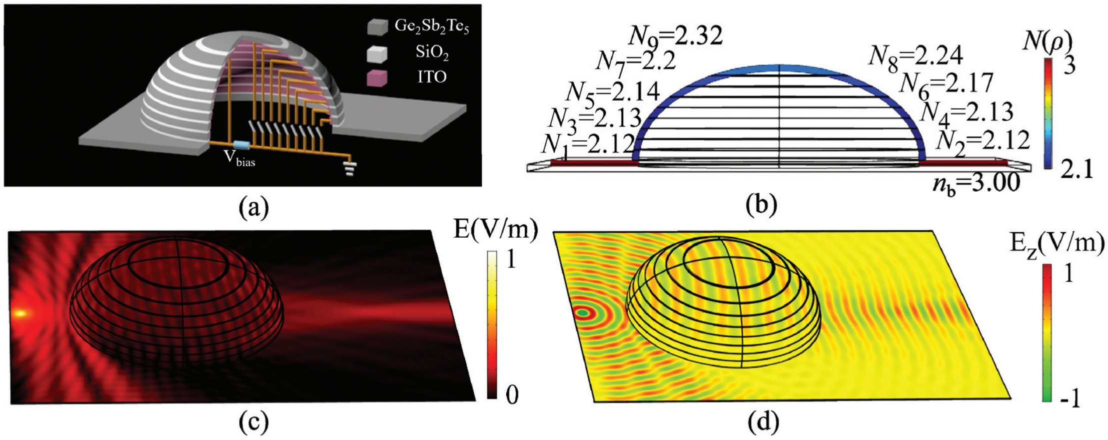

Fig. 2 (a) A scheme of the discretized Rinehart-shaped surface. The ITO line electrodes were on the inside surface of each $Ge_2Sb_2Te_5$ segment. (b) A radial cross-section of the discretized Rinehart-shaped surface with a 9-layered $Ge_2Sb_2Te_5$ dielectric above the amorphous $Ge_2Sb_2Te_5$ ground plane. Distributions of (c) E, and (d) E_z through the surface at λ = 500 nm.

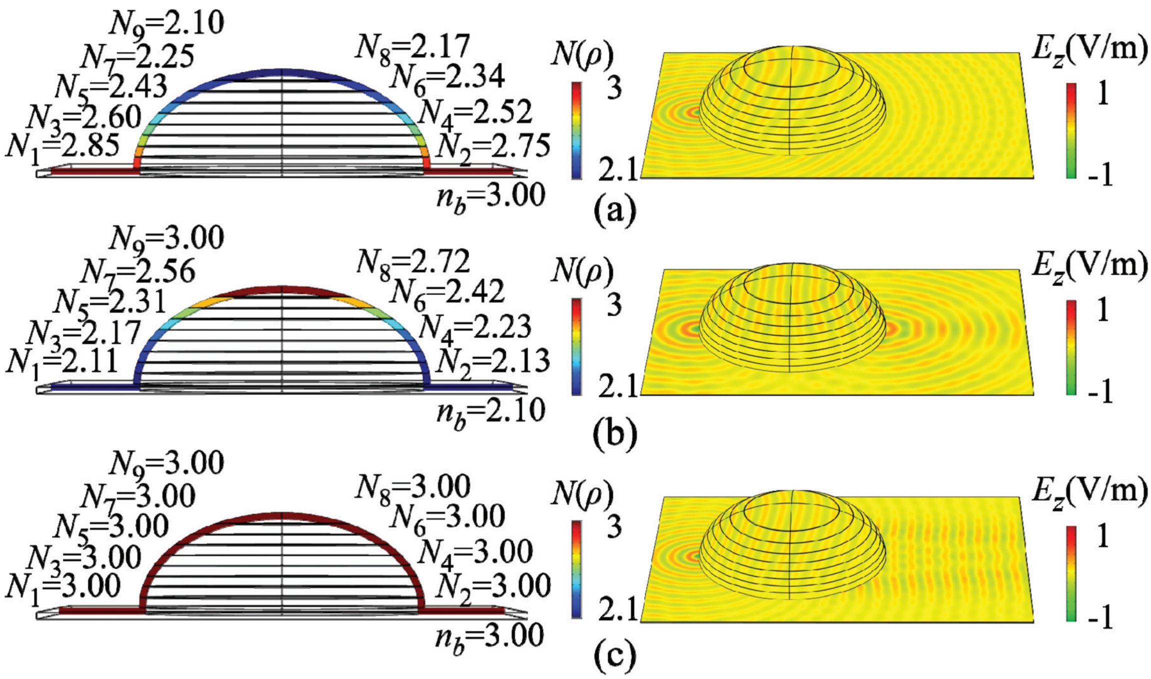

Fig. 3 The left column shows radial cross sections of discretized Rinehart-shaped surfaces with nine distinct layers of the $Ge_2Sb_2Te_5$ dielectric and the right column shows distributions of E_z at the upper surface of constituant $Ge_2Sb_2Te_5$ slabs covering the Rinehart-shaped surface, where a cylindrical wave excited by a point source propagates from left to right for various functions: (a) invisible cloaking, (b) a Maxwell fish-eye lens and (c) a Luneburg lens.

imeter of the lens. It is attained with a refractive index profile expressed as

$$N(\rho) = \frac{2\left(1+\sqrt{1-\rho^2}\right)^{\frac{1}{2}}}{\left(1+\sqrt{1-\rho^2}\right)+\rho^2} \times n_\mathrm{b} \tag{4}$$

where n_b = 2.1 since the $Ge_2Sb_2Te_5$ ground layer is crystalline. For all the above designs, the structure is discretized into nine layers, and the configuration is shown in Fig. 3(b). The Luneburg lens is demonstrated in Fig. 3(c), where the whole structure is in the homogenous amorphous state ($N(\rho)$ = n_b = 3). The simulation results of the above functionalities based on the Rinehart-shaped curvature but without discretization are summarized in the ESI (Fig. S2†). The amorphous $Ge_2Sb_2Te_5$ dielectric becomes crystallized once it is heated above the crystallization temperature of T_C = 433 K and before reaching the melting temperature of T_M = 873 K.[40]

Importantly, the $Ge_2Sb_2Te_5$ can experience several intermediate states, containing regions of both the amorphous and crystalline phases, so-called partial crystallization,[41] which is instrumental for obtaining the gradient refractive index distribution.[42–44] The boundary of the proposed structure can only guide the wave rather than localize the energy relating to the phenomenon. Namely, here the wave was guided by a dielectric curvature with a gradient dielectric constant and not a perfect 2D system.

This shows that an electric current enables the thermal switching of the $Ge_2Sb_2Te_5$ dielectric where rapid heat diffusion, as well as a repeatable energy dose, can control the partial crystallization process.[45] By repeatedly heating the same area of the $Ge_2Sb_2Te_5$ layer with the external stimulus, a continuous change in the refractive index of the $Ge_2Sb_2Te_5$ is achieved.[46,47] The change in the refractive index (or the crystallization proportion) can be verified by infrared reflectivity measurements of the switched area. Eqn (5) describes the effective permittivity of partially crystalline $Ge_2Sb_2Te_5$ by the Lorentz–Lorenz model,[48] which may be broadly tuned *via* the V_{bias} as

$$\frac{\varepsilon_{\text{eff}}(\omega)-1}{\varepsilon_{\text{eff}}(\omega)+2}=j\times\frac{\varepsilon_{\text{crystal}}(\omega)-1}{\varepsilon_{\text{crystal}}(\omega)+2}+(1-j)\times\frac{\varepsilon_{\text{amph}}(\omega)-1}{\varepsilon_{\text{amph}}(\omega)+1} \quad (5)$$

where $\varepsilon_{\text{eff}}(\omega)$ is the effective permittivity of partially crystalline $Ge_2Sb_2Te_5$, $\varepsilon_{\text{crystal}}(\omega)$ and $\varepsilon_{\text{amph}}(\omega)$ are the effective permittivities of crystalline and amorphous $Ge_2Sb_2Te_5$, respectively, and j is the crystallization proportion of $Ge_2Sb_2Te_5$. Thus one can vary the refractive index of the constituent $Ge_2Sb_2Te_5$ slabs to achieve a graded refractive index profile by controlling the crystallization ratio through the t_{bias} applied to each layer (Fig. 2(a)).

As was mentioned above (Fig. 2(a)), the t_{bias} applied to each $Ge_2Sb_2Te_5$ segment can be controlled independently through the separated electrical switch. It thus provides the different crystallization proportions for the different $Ge_2Sb_2Te_5$ slabs. Namely, the achievement of the various crystallization ratios requires the V_{bias} to hold the $Ge_2Sb_2Te_5$ above the T_C, but below the T_M for the different time durations (t_d). The specific temporal changes in the temperatures of the $Ge_2Sb_2Te_5$ constituent curved layers for each TO functionality are displayed in Fig. 4. The two fundamental state transitions of crystallization and reamorphization take place at different temperatures and time scales. Herein, we focus on reversible switching using an electrically triggered state transition. The thermal properties of the $Ge_2Sb_2Te_5$ material utilized for the model can be found in ref. 49.

We start from the invisible cloaking (stage-I). First, the numerical simulation shows that the temperature within the as-deposited amorphous $Ge_2Sb_2Te_5$ dielectric layer increases with t_{bias} under V_{bias} = 1 V. It can exceed the amorphous-to-crystalline transition temperature of T_C = 433 K after $t_c \sim 4$ ns, where the planar ground layer is amorphous $Ge_2Sb_2Te_5$ (n_b = 3). To crystallize the $Ge_2Sb_2Te_5$ completely, a follow-up annealing procedure is carried out to provide sufficient thermal energy to maintain the temperature above T_C but below T_M for ~50 ns.[50] Through time controlled external heating, one can manage the crystallization proportions and thus modulate the refractive index of each constituent $Ge_2Sb_2Te_5$ band to approximate the required gradient profile (the left column of Fig. 3(a)). The corresponding crystallization

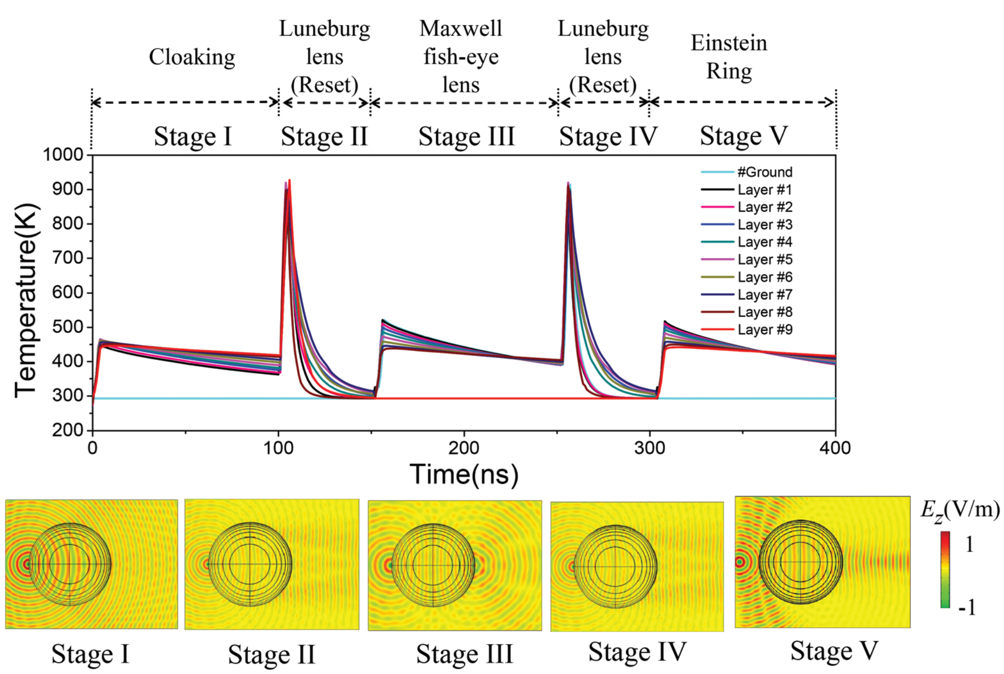

Fig. 4 A time dependent temperature distribution of the $Ge_2Sb_2Te_5$ layers for invisible cloaking (stage I), the Luneburg lens (stage II), the Maxwell fish-eye lens (stage III), the Luneburg lens (stage IV), and the Einstein ring (stage V). Bottom panels: Distributions of E_z from stage I to stage V.

proportion (j) and time durations (t_d) for each $Ge_2Sb_2Te_5$ slab are shown in the ESI (Table S1†). Note that the V_{bias} linking to the ground layer is off (disconnected) to maintain the as-deposited amorphous state. The temperatures of the crystalline $Ge_2Sb_2Te_5$ layers start dropping down to room temperature once the bias voltage (V_{bias} = 1 V) is off (disconnected), due to heat dissipation into the surrounding air.

In stage II, all of the partially and fully crystalline $Ge_2Sb_2Te_5$ bands are reset to the amorphous state (the left column of Fig. 3(c)), in which the Luneburg lens is achieved. To amorphize the $Ge_2Sb_2Te_5$, the crystal lattice needs to be molten and afterwards quenched to room temperature to prevent any recrystallization of the atomic structure. A bias time of 12 ns for the V_{bias} = 3 V is sufficient to initiate such a melt-quenching process. By switching off the V_{bias} = 3 V, subsequent fast cooling can decrease the temperature and quench the melt into the amorphous state. It should be pointed out that the crystal lattice of a $Ge_2Sb_2Te_5$ layer requires a period to relax from the amorphous to the crystalline state, resulting in a longer duration of phase alternation than the time needed for melt-quenching the lattice into the amorphous state.

In stage III, we then proceed to demonstrate the time dependent temperature distributions for the Maxwell fish-eye lens. The conditions, j as well as t_d, of each $Ge_2Sb_2Te_5$ layer are summarized in the ESI (Table S2†), and satisfy the refractive index shown in the left column of Fig. 3(b). Herein, the V_{bias} linking to both the ground layer and layer 1 is "on" to fully crystallize the $Ge_2Sb_2Te_5$ (n_b = 2.1) in t_d = 50 ns, and layer 9 is fixed in the amorphous state. In stage IV, V_{bias} = 3 V is again adopted to reamorphize all the $Ge_2Sb_2Te_5$ layers (from the ground planar layer to the top curved layer) in 12 ns.

Finally, the time-dependent temperature distributions of the $Ge_2Sb_2Te_5$ layers to achieve the Einstein ring are demonstrated in stage V with j and t_d shown in the ESI (Table S3†). A full recorded movie of the features discussed above has been provided in the ESI video.† A detailed description of the movie can be found in Section 7 of the ESI.†

Another interesting finding is that our device can cover most of the visible region (from 450 to 650 nm), over which the curvature precisely creates the collimating beam, cloaking and Luneburg lens performances, although the guided-wave implementation was initially designed to operate at λ = 500 nm (Fig. S7–S9 of the ESI†). This indicates that our reconfigurable active device is precise in reconstructing the guided-wave fronts over a broad bandwidth in the visible region. It is worth mentioning that although this work itself is not experimental, the theoretical analysis is built upon the measured dielectric constant of $Ge_2Sb_2Te_5$,[27,51] showing the possibility of real-world applications. We also developed a thermoelectric model to examine the temporal variation of the temperature of each constituent $Ge_2Sb_2Te_5$ curved slab. It shows that, by controlling the bias time (t_{bias}) of the applied V_{bias}, the different $Ge_2Sb_2Te_5$ layers can be crystallized in various proportions, resulting in a predetermined refractive index gradient distribution to achieve the desired functions in nanoseconds. Thus, our proposed structure can rapidly manipulate the wavefront of guided-waves in the visible region. This is highly advantageous for TO systems where ultrafast reconfigurability and versatile reprogrammable functions are major concerns. Given that the phase transition is a transient heating procedure and the $Ge_2Sb_2Te_5$ cannot efficiently localise the E-field, in the model we do not consider the nonlinearity of the $Ge_2Sb_2Te_5$ at high temperatures.

3. Conclusions

In conclusion, we have studied the feasibility of tailoring the propagation of guided-waves by solely modulating the chalcogenide in a Rinehart-shaped curvature waveguide. It shows that the electrified surface composed of $Ge_2Sb_2Te_5$ curved slabs can be used as versatile nonplanar TO devices. It can control the wave propagation in various ways and operate in the visible region by triggering the bias voltages to $Ge_2Sb_2Te_5$ segments. The unification of the conventional TO technique with the ultrafast state transition of $Ge_2Sb_2Te_5$ is expected to establish a new paradigm in real-time multifunctional systems. It may offer an unexploited means for arbitrary and dynamic focusing of light, light shaping and cloaking across most of the visible region, and increasing integration with other structures to create versatile and advanced functions. We also envisage that the interesting interactions between photonic nanostructures and the recently developed phase change material family of Ge–Sb–Te alloys could lead to further exciting developments in physics and new roles in the field of atomic-scale photonics.

Conflicts of interest

There are no conflicts to declare.

Acknowledgements

This work was supported by the National Natural Science Foundation of China (Grant No. 61172059, 51302026), the International Science & Technology Cooperation Program of China (Grant No. 2015DFG12630) and the Program for Liaoning Excellent Talents in University (Grant No. LJQ2015021).

References

1 X. Wan, X. Shen, Y. Luo and T. J. Cui, *Laser Photonics Rev.*, 2014, **8**, 757–765.
2 K. Chen, Y. Feng, F. Monticone, J. Zhao, B. Zhu, T. Jiang, L. Zhang, Y. Kim, X. Ding, S. Zhang, A. Alù and C.-W. Qiu, *Adv. Mater.*, 2017, **29**, 1606422.
3 S. Liu and T. J. Cui, *Adv. Opt. Mater.*, 2017, **5**, 1700624.
4 Z. Wu, K. Chen, R. Menz, T. Nagao and Y. Zheng, *Nanoscale*, 2015, **7**, 20391–20396.

5 X. Zhao, C. Yuan, L. Zhu and J. Yao, *Nanoscale*, 2016, **8**, 15273–15280.
6 L. Lin, Y. Lu, M. Yuan, F. Shi, H. Xu and Y. Chen, *Nanoscale*, 2017, **9**, 18482–18489.
7 T. Driscoll, H. T. Kim, B. G. Chae, B. J. Kim, Y. W. Lee, N. M. Jokerst, S. Palit, D. R. Smith, M. Di Ventra and D. N. Basov, *Science*, 2009, **325**, 1518–1521.
8 C. H. Chu, M. L. Tseng, J. Chen, P. C. Wu, Y.-H. Chen, H.-C. Wang, T.-Y. Chen, W. T. Hsieh, H. J. Wu, G. Sun and D. Ping Tsai, *Laser Photonics Rev.*, 2016, **10**, 986–994.
9 H. S. Ee and R. Agarwal, *Nano Lett.*, 2016, **16**, 2818–2823.
10 L. Zhang, S. Mei, K. Huang and C.-W. Qiu, *Adv. Opt. Mater.*, 2016, **4**, 818–833.
11 K. Liu, X. Zeng, S. Jiang, D. Ji, H. Song, N. Zhang and Q. Gan, *Nanoscale*, 2014, **6**, 5599–5605.
12 Y. Yao, R. Shankar, M. A. Kats, Y. Song, J. Kong, M. Loncar and F. Capasso, *Nano Lett.*, 2014, **14**, 6526–6532.
13 Y. Qu, Q. Li, K. Du, L. Cai, J. Lu and M. Qiu, *Laser Photonics Rev.*, 2017, **11**, 1700091.
14 M. Liu, X. Yin, E. Ulin-Avila, B. Geng, T. Zentgraf, L. Ju, F. Wang and X. Zhang, *Nature*, 2011, **474**, 64.
15 J. Deng, J. Fu, J. Ng and Z. Huang, *Nanoscale*, 2016, **8**, 4504–4510.
16 X. Yin, M. Schäferling, A.-K. U. Michel, A. Tittl, M. Wuttig, T. Taubner and H. Giessen, *Nano Lett.*, 2015, **15**, 4255–4260.
17 Y. Liu and X. Zhang, *Nanoscale*, 2012, **4**, 5277–5292.
18 R. C. Mitchell-Thomas, T. M. McManus, O. Quevedo-Teruel, S. A. R. Horsley and Y. Hao, *Phys. Rev. Lett.*, 2013, **111**, 213901.
19 R. C. Mitchell-Thomas, O. Quevedo-Teruel, T. M. McManus, S. A. R. Horsley and Y. Hao, *Opt. Lett.*, 2014, **39**, 3551–3554.
20 M. S. Kim, B. V. Lahijani, N. Descharmes, J. Straube, F. Negredo, C. Rockstuhl, M. Hayrinen, M. Kuittinen and H. P. Herzig, *ACS Photonics*, 2017, **4**, 1477–1483.
21 R. Macêdo, T. Dumelow and R. L. Stamps, *ACS Photonics*, 2016, **3**, 1670–1677.
22 M. Rahm, D. Schurig, D. A. Roberts, S. A. Cummer, D. R. Smith and J. B. Pendry, *Photon. Nanostruct.: Fundam. Applic.*, 2008, **6**, 87–95.
23 Y. G. Ma, C. K. Ong, T. Tyc and U. Leonhardt, *Nat. Mater.*, 2009, **8**, 639–642.
24 B. S. Lee and J. R. Abelson, *J. Appl. Phys.*, 2005, **97**, 093509.
25 P. Hosseini, C. D. Wright and H. Bhaskaran, *Nature*, 2014, **511**, 206–211.
26 B. J. Eggleton, B. L. Davies and K. Richardson, *Nat. Photonics*, 2011, **5**, 141–148.
27 K. Shportko, S. Kremers, M. Woda, D. Lencer, J. Robertson and M. Wuttig, *Nat. Mater.*, 2008, **7**, 653–658.
28 X. Yin, T. Steinle, L. Huang, T. Taubner, M. Wuttig, T. Zentgraf and H. Giessen, *Light: Sci. Appl.*, 2017, **6**, e17016.
29 P. Li, X. Yang, T. W. W. Maß, J. Hanss, M. Lewin, A.-K. U. Michel, M. Wuttig and T. Taubner, *Nat. Mater.*, 2016, **15**, 870–875.
30 C. H. Chu, M. L. Tseng, J. Chen, P. C. Wu, Y.-H. Chen, H.-C. Wang, T.-Y. Chen, W. T. Hsieh, H. J. Wu, G. Sun and D. P. Tsai, *Laser Photonics Rev.*, 2016, **10**, 1600106.
31 C. Sheng, R. Bekenstein, H. Liu, S. Zhu and M. Segev, *Nat. Commun.*, 2016, **7**, 10747.
32 J. C. Minano, *Opt. Express*, 2006, **14**, 9627–9635.
33 J. Sochacki, *Appl. Opt.*, 1984, **23**, 4444–4449.
34 M. Šarbort and T. Tyc, *J. Opt.*, 2012, **14**, 075705.
35 J. N. Hewitt, E. L. Turner, D. P. Schneider, B. F. Burke, G. I. Langston and C. R. Lawrence, *Nature*, 1988, **333**, 537–540.
36 L. J. King, N. Jackson, R. D. Blandford, M. N. Bremer, I. W. A. Browne, A. G. De Bruyn, C. Fassnacht, L. Koopmans, D. Marlow and P. N. Wilkinson, *Mon. Not. R. Astron. Soc.*, 1998, **295**, L41–L44.
37 K. S. Kunz, *J. Appl. Phys.*, 1954, **25**, 642.
38 M. Wuttig, H. Bhaskaran and T. Taubner, *Nat. Photonics*, 2017, **11**, 465–476.
39 J. D. J. Ingle and S. R. Crouch, *Spectrochemical Analysis*, Prentice Hall, New Jersey, 1988.
40 B. Gholipour, J. Zhang, K. F. MacDonald, D. W. Hewak and N. I. Zheludev, *Adv. Mater.*, 2013, **25**, 3050–3054.
41 B. S. Lee, G. W. Burr, R. M. Shelby, S. Raoux, C. T. Rettner, S. N. Bogle, K. Darmawikarta, S. G. Bishop and J. R. Abelson, *Science*, 2009, **326**, 980–984.
42 C. M. Chang, C. H. Chu, M. L. Tseng, H.-P. Chiang, M. Mansuripur and D. P. Tsai, *Opt. Express*, 2011, **19**, 9492–9504.
43 M. L. Tseng, B. H. Chen, C. H. Chu, C. M. Chang, W. C. Lin, N.-N. Chu, M. Mansuripur, A. Q. Liu and D. P. Tsai, *Opt. Express*, 2011, **19**, 16975–16984.
44 Y. Yina, T. Noguchi, H. Ohno and S. Hosaka, *Appl. Phys. Lett.*, 2009, **95**, 133503.
45 D. Loke, T. Lee, W. Wang, L. Shi, R. Zhao, Y. Yeo, T. Chong and S. Elliott, *Science*, 2012, **336**, 1566.
46 C. D. Wright, Y. Liu, K. I. Kohary, M. M. Aziz and R. J. Hicken, *Adv. Mater.*, 2011, **23**, 3408–3413.
47 Y. Liu, M. M. Aziz, A. Shalini, C. D. Wright and R. J. Hicken, *J. Appl. Phys.*, 2012, **112**, 123526.
48 D. E. Aspnes, *Am. J. Phys.*, 1982, **50**, 704–709.
49 T. Cao, J. X. Bao, L. B. Mao, T. H. Zhang, A. Novitsky, M. Nieto-Vesperinas and C. W. Qiu, *ACS Photonics*, 2016, **3**, 1934–1942.
50 N. Yamada, E. Ohno, N. Akahira, K. Nishiuchi, K. Nagata and M. Takao, *Jpn. J. Appl. Phys.*, 1987, **26**, 61–66.
51 W. Dong, Y. Qiu, X. Zhou, A. Banas, K. Banas, M. B. H. Breese, T. Cao and R. E. Simpson, *Adv. Opt. Mater.*, 2018, 1701346, DOI: 10.1002/adom.201701346.